Contrib Mineral Petrol (2015) 169:52
DOI 10.1007/s00410-015-1146-3

ORIGINAL PAPER

Weathering crusts on peridotite

Kurt Bucher[1] · **Ingrid Stober**[1] · **Hiltrud Müller-Sigmund**[1]

Received: 2 November 2014 / Accepted: 12 May 2015 / Published online: 4 June 2015

Abstract Chemical weathering of dark-green massive peridotite, including partly serpentinized peridotite, produces a distinct and remarkable brown weathering rind when exposed to the atmosphere long enough. The structure and mineral composition of crusts on rocks from the Ronda peridotite, Spain, have been studied in some detail. The generic overall weathering reaction serpentinized peridotite + rainwater = weathering rind + runoff water describes the crust-forming process. This hydration reaction depends on water supply from the outcrop surface to the reaction front separating green peridotite from the brown crust. The reaction pauses after drying and resumes at the front after wetting. The overall net reaction transforms olivine to serpentine in a volume-conserving replacement reaction. The crust formation can be viewed as secondary serpentinization of peridotite that has been strongly altered by primary hydrothermal serpentinization. The reaction stoichiometry of the crust-related serpentinization is preserved and reflected by the composition of runoff waters in the peridotite massif. The brown color of the rind is caused by amorphous Fe(III) hydroxide, a side product from the oxidation of Fe(II) released by the dissolution of fayalite component in olivine.

Keywords Weathering crust · Peridotite · Fe hydroxide · Olivine hydration · Peridotite water

Communicated by Chris Ballhaus.

✉ Kurt Bucher
bucher@uni-freiburg.de

[1] Mineralogy and Petrology, University of Freiburg, Albertstr. 23b, 79104 Freiburg, Germany

Introduction

Green peridotite rocks are typically covered with brown weathering rinds of variable thickness. The characteristic brown crusts help to recognize outcrops of ultramafic rock at the erosion surface from a long distance to the delight of the experienced field geologist. Stunning examples from northern Norway and southern Spain (Fig. 1) show that these crusts cover ultramafic rocks in different geodynamic settings at all latitudes. The crusts are intrinsically associated with the presence of olivine in the weathering rock irrespective of local climate and weathering conditions. The thickness of the crusts shows considerable variation at a given locality (Fig. 2), suggesting that a major controlling factor is the detailed permeability structure of the rock that is the microstructure (texture) of the rock. The brown weathering crusts on peridotite have been reported and described from localities worldwide (Lauder 1965; Evzerov et al. 2007; Bucher-Nurminen 1991; Lindahl and Nilsson 2008; Nilsson et al. 2005; Bucher 2012; Yoshida et al. 2011). In wet and warm climates, peridotite weathering may form very deep laterite-type soils (several meters) and Ni deposits (Lelong et al. 1976; Sagapoa et al. 2011). Intense weathering of peridotite may form a series of rather unusual secondary minerals from olivine including iddingsite, opal, chalcedony, magnesite, nontronite, and kaolinite (Edwards 1938; Boev et al. 2009). Note that iddingsite is not a mineral but a mixture of phases, crystalline and amorphous, pseudomorphing olivine (Smith et al. 1987). The brown crusts reported here are different from iddingsite pseudomorphs as regards textures and details of crust-forming processes. Rusty-colored weathering rinds occur on other types of rocks including gneiss and schists (Dixon et al. 2002), but in contrast to peridotite, the rusty surface is typically caused by sulfide weathering. The minerals and

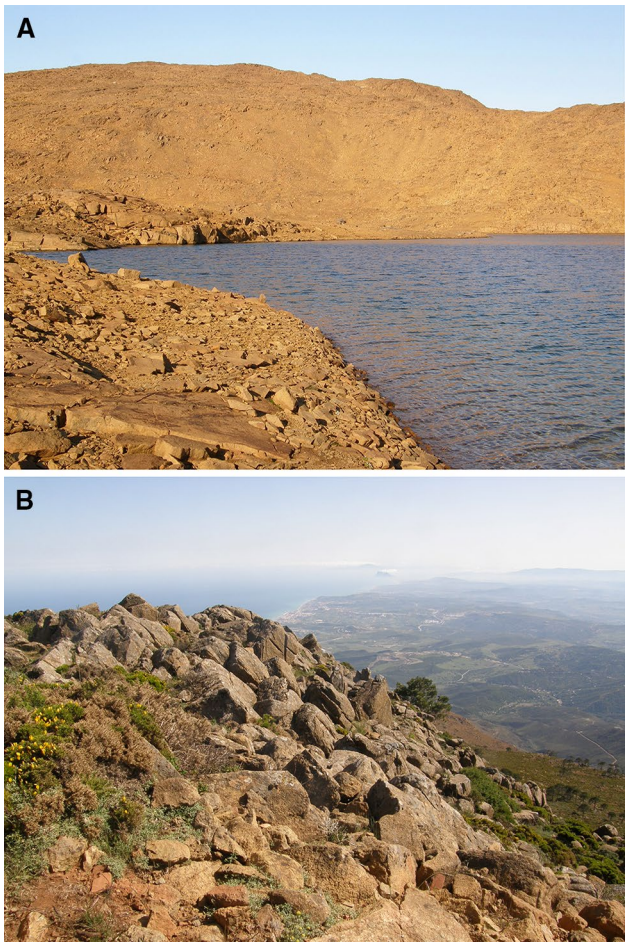

Fig. 1 **a** Reinfjorden peridotite, northern Norway (71° North). The ultramafic rocks are part of the Seiland igneous complex and as such represents the basal parts of layered gabbroic intrusions. The *yellow* crust covering the *dark-green* peridotite is only about 1–2 mm thin. **b** Ronda Peridotite at Pico de los Reales (1450 m) with view to Gibraltar and the Rif mountains of Morocco in the South. The *yellow–brown* crust on the peridotite is 20–30 mm thick. Note the difference between the vegetation cover of peridotite at 71° North and the southern Mediterranean

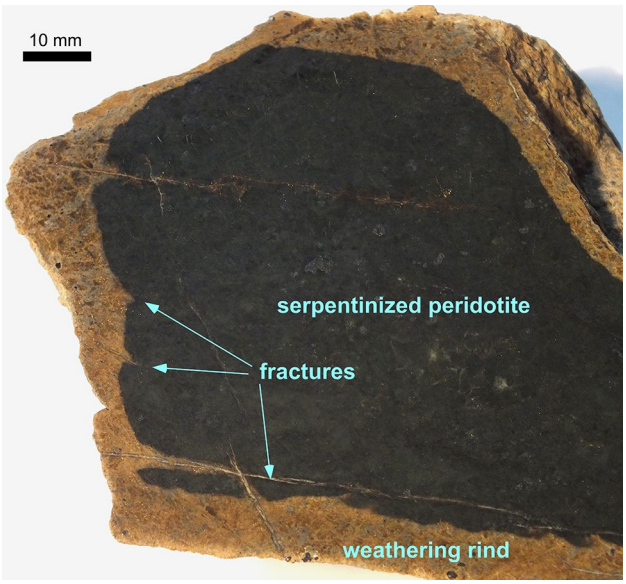

Fig. 2 Sample of serpentinized peridotite from Forrhaugen, Kvaløya, northern Norway showing a *brown* weathering crust ranging from 1 to 10 mm in thickness. The thickness of the *brown* rind is visibly influenced by small fractures providing enhanced permeability

chemical composition of these sulfide-derived rinds have been studied in some detail (Durocher and Schindler 2011).

Brown crusts on peridotite in moderate and cold climates are typically relatively thin (Figs. 1, 2). Solid SiO_2 (e.g., amorphous silica, opal, quartz) is usually not present in these crusts. In this study, we show that the processes forming the crusts and their mineralogy are remarkably complex. What is clear is that the process of crust formation is an oxidation process that oxidizes Fe^{2+} in olivine to Fe^{3+} in the brown material. The oxidation is associated with hydration of olivine to various hydrates including serpentine and iron hydroxides. Specifically, we present an analysis of the weathering crusts on the Ronda Peridotite in Southern Spain (Fig. 3) and discuss the processes that may form the crusts.

Geological setting

The Ronda Peridotite is the largest peridotite outcrop in the world, extending for more than 70 km in E–W direction, and it covers more than 300 m^2 surface outcrops (Dikey et al. 1979). It forms a part of the Alpujárride thrust sheet in the Betic Cordillera in southern Spain. The primary peridotite contains predominantly olivine and some orthopyroxene as main minerals and minor amounts of clinopyroxene. The distribution of aluminum-bearing minerals in the peridotite massive is strongly zoned (Obata 1980) with plagioclase in the structurally highest part, spinel in the main volume of the body, and garnet in the structurally deepest parts of the peridotite (Fig. 4a, d). The peridotite is generally considerably to massively serpentinized. The degree of serpentinization increases in places toward the thrust contacts with the overthrusted sedimentary units. In the main body of the Ronda peridotite, olivine and serpentine occur in similar modal amounts (Fig. 4b, c). Locally, the peridotite contains abundant veins (dykes) of garnet pyroxenite. The petrologic significance of garnet in the ultramafic rocks, the internal structure of the Ronda peridotite, and the mechanism of tectonic emplacement of the peridotite in the Betic nappes stack have been of considerable interest (Schubert 1977, 1982; Van der Wal and Vissers 1996; Mazzoli and Martin Algarra 2011).

The peridotite is covered with the characteristic yellow–brown weathering rind. The thickness of the rinds is

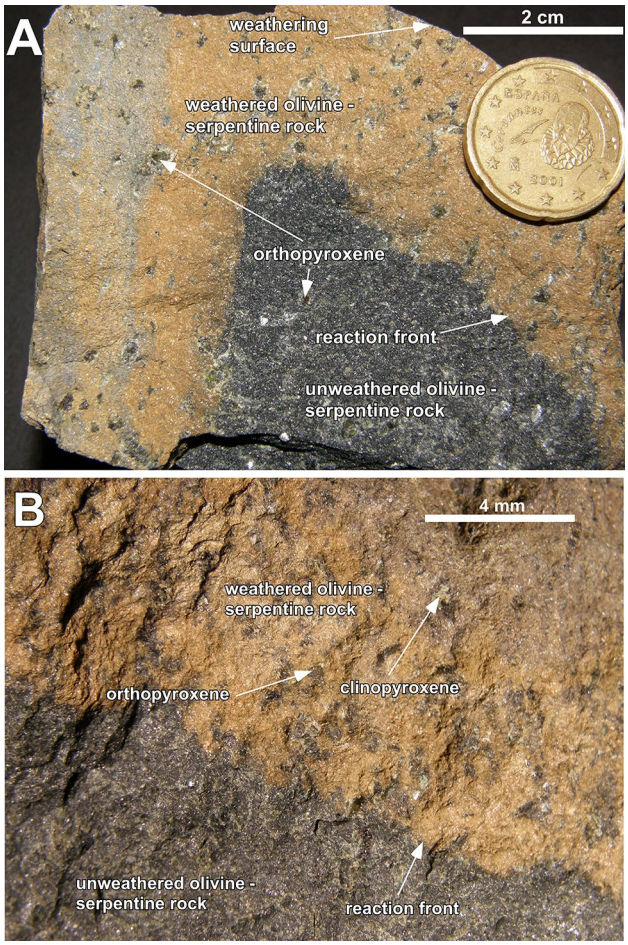

Fig. 3 **a** Peridotite rock sample from the Sierra Palmitera showing a 25-mm-*thick brown* weathering rind. The *dark-green* part is "fresh" serpentinized peridotite of the type shown on Fig. 4b. At the surface exposed to the atmosphere a *brown* crust is present. The crust-producing reaction migrates into the "fresh" rock along a very sharp reaction front. **b** Close up of the reaction front of sample shown **a**

typically about 2–3 cm and does not show much variation. The rind development is related to the exposure of the peridotite to surface conditions with rainwater, atmospheric CO_2, and O_2. However, the modal mineral content, the microstructure (texture), and the composition of the rocks control to a large extent the weathering rind development after exposure to the atmosphere in addition to the atmospheric parameters such as annual rainfall, average temperature and frequency and duration of wetting, and drying cycles.

Rock and water samples

The rock samples used for this study were collected at road cuts along the road from Estepona at the Mediterranean Sea and the town Jubrique in the mountains NNW of Estepona. Some samples have been collected along the dead end road to Pico Reales (1450 m), the highest peak in the massif (Fig. 1b). Some excellent outcrops can also be visited in the Sierra Palmitera along the road from San Pedro to Ronda. All samples show very similar structural features and weathering rinds of similar thickness.

About two to three cm below the weathering surface exposed to rain and the atmosphere, "fresh" dark-green peridotite is present (Fig. 3). The green matrix contains partially serpentinized olivine. Particularly prominent are occasional large (>2 mm) grains of orthopyroxene. The orthopyroxene grains are rather euhedral and become prominently visible in the weathered brown part of the rock. Orthopyroxene seems to be a passive player in the rind-forming process, as no reaction textures are related to the orthopyroxene grains. Similarly, primary Cr-spinel and secondary magnetite are exposed at the weathering surface without any sign of being affected by weathering reactions.

The rind-forming process causes a sharp reaction front separating brown and green rock (Figs. 2, 3). The reaction(s) are probably driven by the interaction of surface water (rain) and atmospheric gases with olivine, which is not a stable phase at surface conditions (Bucher and Grapes 2011). If so, the process may release reaction products in the form of solutes to the surface runoff. Therefore, we collected five water samples from creeks at the flanks of Pico Reales. Sampling took place in May 2010 and May 2011. At this time of the year, surface runoff is between the winter wet period and the summer dry period, when most of the creeks run dry. The sampled catchments at Pico Reales are exclusively in peridotite bedrock and a very thin layer of peridotite derived soil. A small fraction of the surface area is covered with pyroxenite. However, because pyroxenite (pyroxene) is much less reactive than peridotite (olivine) (Lasaga 1984; Lasaga et al. 1994), the water composition may largely reflect the consequences of the surface water–olivine interaction. The riverbeds where the samples have been collected show peridotite bedrock exposures and pebbles and sand of the same material. No sinter formations or any other precipitates of potential secondary reaction products such as carbonates, silica, or clay have been detected or observed in the rivers.

Petrography

Peridotite samples

Dark-green peridotite consists predominantly of olivine and serpentine. The primary olivine forms a matrix of coarse grains that are broken by a network of later serpentine veinlets. The serpentinization veinlets leave isolated relics of unreacted olivine grains of various sizes (Fig. 4b, c).

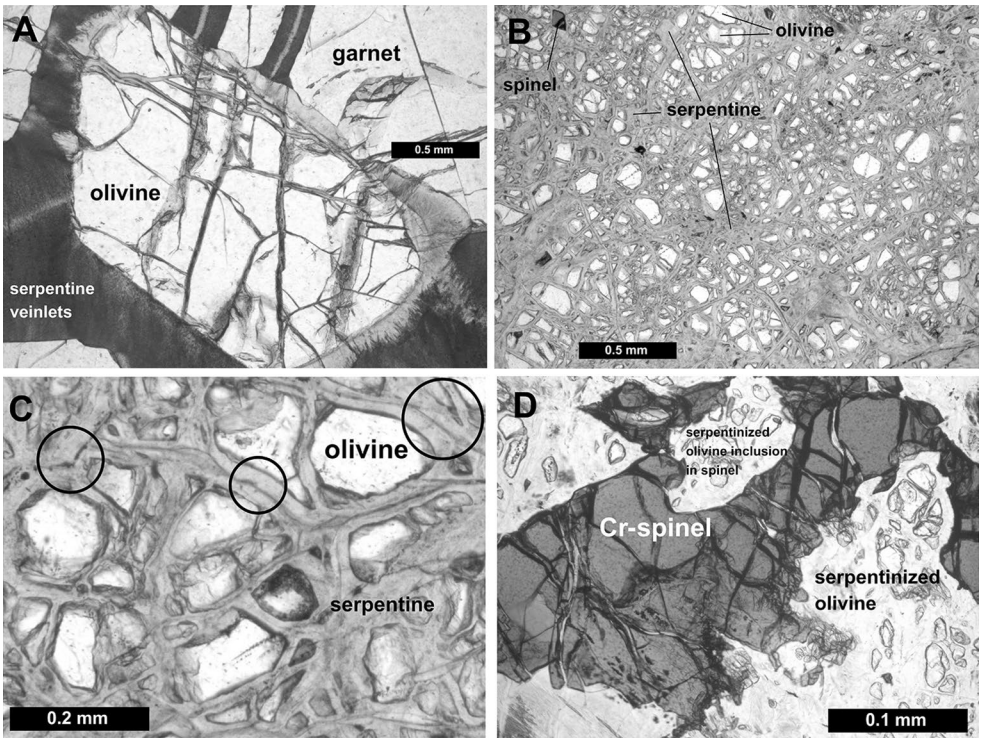

Fig. 4 Photomicrographs of textures of unweathered green serpentinized peridotite: **a** Garnet peridotite from the Ronda peridotite (along the Jubrique road to Reales). Composition of coexisting garnet and olivine is given on Table 1. **b** Serpentinized spinel peridotite from the Ronda peridotite. The sample is strongly serpentinized and contains 65 % serpentine and 30 % olivine and 5 % other minerals including Cr-rich spinel. The sample shown here represents the "fresh" green peridotite before it reached at the erosion surface. **c** Symmetrical serpentine veinlets in Ronda peridotite. *Black circles* examples of veinlets: the centers of the veinlets contain a *black* opaque very fine-grained phase probably magnetite. Minerals across the veinlets are: olivine–serpentine (lizardite)–magnetite (in the suture, center of the veinlet). **d** Spinel peridotite from the Ronda peridotite (along the Jubrique road to Reales). Olivine is strongly serpentinized in the sample; *spinel* shows no chloritization along fractures

The distribution of the olivine relics is rather regular in parts of the samples. However, it may also be heterogeneous with large olivine grains in one part of the sample and almost complete serpentinization in others. The serpentinization veins measure typically 0.01–0.1 mm across with a dark porous suture zone in the center of the vein. This seam is locally stained by small opaque grains identified as magnetite (Fig. 4c). The olivine relics are embedded in a clear, light-colored serpentine zone. Serpentine trends perpendicular to the central suture of the veins. Toward the suture, the serpentine zones become gradually darker, and they are speckled with very small opaque "dust", probably also magnetite. The total amount of magnetite present is close to 5 vol.%.

Clinopyroxene is present in small amounts (<5 vol.%). The mineral has a grain size of 3–6 mm. It appears that it is texturally unrelated to the serpentine veinlets and unaffected by the serpentinization process. Locally clinopyroxene is overgrown by fibrous Ca-amphibole.

Red–brown anhedral Cr-rich spinel of maximum 3-mm size occurs throughout the sampled rocks of spinel peridotite (~5 vol.%). Most grains are much smaller, though. The large grains are texturally interstitial to the olivine matrix. The spinels are fractured and transected by micro-veins, but not chloritized and also not rimmed with magnetite or otherwise affected by the serpentization process (Fig. 4d). Samples at the base of the Ronda peridotite massif collected at road cuts above Jubrique contain garnet instead of spinel (Fig. 4a).

Brown weathering rinds

The petrography of the brown rinds is almost identical to that of the green peridotite rocks. There is one minor but significant difference, however. In the rinds, a brown stain is present predominantly along the central sutures of the serpentine veinlets (Fig. 5) but also in the serpentine zones along the central sutures. The distribution and modal abundance of the brown material is uniform across the weathering rind, which we believe, is a significant observation. The brown pigment is not present in the immediate vicinity of the relic olivine grains (Fig. 5a, b). The brown material

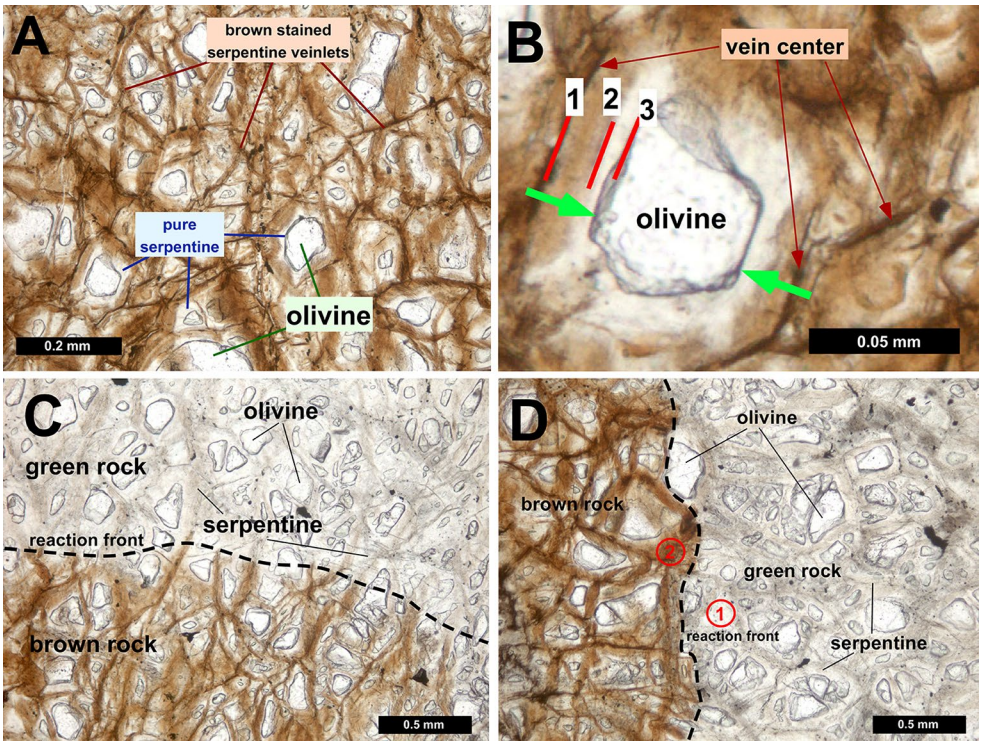

Fig. 5 Photomicrographs of textures of brown weathering rind and reaction front: **a** *Brown* weathering rind on serpentinized Ronda peridotite. It shows *brown* stain of serpentinite veinlets in the weathering rind. **b** The *brown* stain occurs in the central parts of the serpentine veinlets only; the very close vicinity of olivine is free of the brown weathering product. Zone boundaries: 1 = central suture of veinlet, 2 = oxidation front, first occurrence of Fe(III) hydroxide, 3 = olivine–serpentine contact. *Green arrows* = site of olivine-serpentine transformation. **c** Very sharp and localized reaction front separating the brown weathering rind from "fresh" serpentinized Ronda peridotite. The brown stain occurs in the central parts of the serpentine veinlets only. **d** Sharp reaction front of the weathering reaction. 1 = Green serpentinized peridotite, 2 = brown crust

does not form visible crystals identifiable with the microscope. The boundary between rock domains with and without the brown stain is sharp and corresponds to the green–brown boundary visible on rock samples (Fig. 3). The occurrence of the first brown stain approaching from the green side is clearly related to the central suture of the serpentinite veinlets (Fig. 5c, d). Some porosity occurs near the green–brown boundary (locally up to 5 %). The porosity is partly and locally sealed by Fe hydroxide and oxide precipitates (Fig. 6). The highly reflective Fe material is not present in the same texture in the green rock where dispersed magnetite is present resulting from the original hydrothermal serpentinization process.

Composition of minerals and rocks

Methods

Quantitative mineral analysis were performed at the Institute of Mineralogy, University of Freiburg, using a CAMECA SX 100 electron microprobe equipped with five WD spectrometers and one ED detector with an internal PAP correction program (Pouchou and Pichior 1991). Major and minor elements were determined at 15-kV accelerating voltage and 10-nA beam current with counting time up to 20 s. Natural and synthetic standards were used for calibration. Whole rock analyses were performed by standard X-ray fluorescence (XRF) techniques, using a Philips PW 2404 spectrometer. Pressed powder and Li borate-fused glass disks were prepared to measure contents of trace and major elements, respectively. The raw data were processed with the standard XR-55 software of Philips. Relative standard deviations are <1 and <4 % for major and trace elements, respectively. Loss on ignition was determined by heating at 1100 °C for 2 h.

Minerals

Obata (1980) reported the compositions of minerals from 12 samples from the Ronda peridotite including data from spinel peridotite from the Pico los Reales area. Olivine ranges in composition from Fo 88 to Fo 92 (mol %). The reported mean forsterite content is close to 90 %. For this

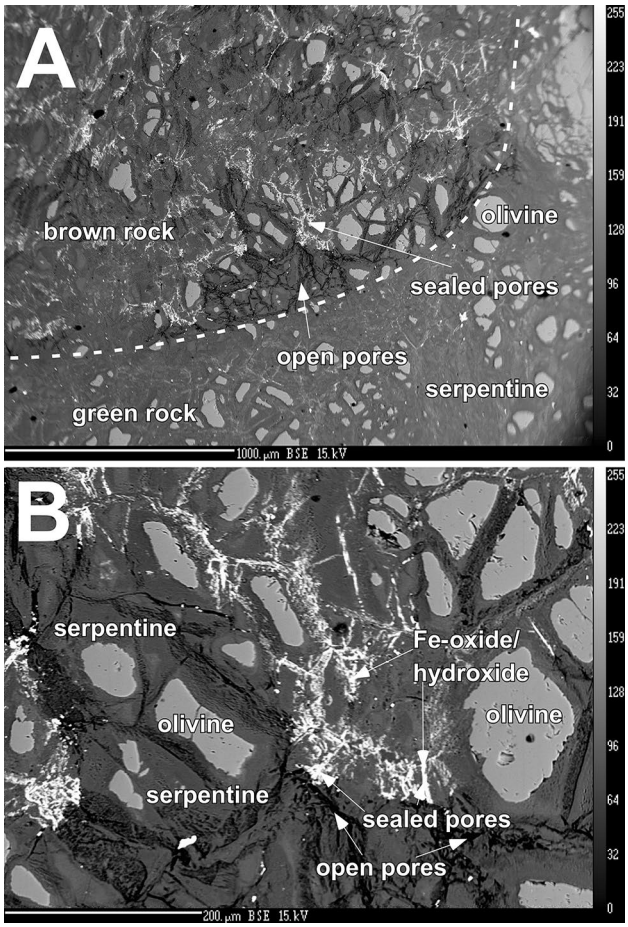

Fig. 6 **a** BSE image across the green–brown rock boundary showing the porosity structure near the reaction front. **b** BSE image showing details of the porosity structure inside the brown rock

study, we analyzed the minerals of garnet peridotite and spinel peridotite (Table 1). Olivine inclusions in garnet contain 88.5 mol % forsterite, about 10 % fayalite, and 0.5 mol % tephroite component. All other components, including Ni-olivine, are very low (<0.05 mol %). Serpentine is probably present as lizardite variety because of its relatively high iron content, although chrysotile can be quite Fe-rich too. The low total may suggest, however, that the Fe is not exclusively present as Fe(II) in the structure of the serpentine, but some Fe could be present as Fe-bearing brucite (Mumpton and Thompson 1966). Serpentine has an X_{Mg} of close to 0.94 (Table 1). Clinopyroxene contains about 3–5 wt% Al_2O_3 and 1–1.5 wt% Cr_2O_3 corresponding to significant Tschermak components (Obata 1980). X_{Mg} of Cpx is about 0.92. Cr-spinel of the examined rocks contains between 8.3 and 35 wt% Cr_2O_3, depending on grain size of the spinels (Obata 1980). Our samples contain spinel with 25–27 wt% Cr_2O_3 (Table 1). X_{Mg} varies from 0.66 to 0.78. Garnet in the sampled garnet-bearing peridotite is composed of 71 % pyrope, 15 % almandine, 12.5 % grossular, 0.5 % spessartine component, and 1 % uvarovite component (Table 1). Kelyphite rims and veins replacing garnet are composed of Ca-amphibole with 0.7 wt% Cr_2O_3.

The brown stain of the weathering rind could not be analyzed by the electron beam micro-analyzer. Brown domains on the polished sections give an increased Fe signal. However, the analyses are close to serpentine. We attempted to separate the brown material from serpentine using standard mineral separation routines. The brown material could be concentrated by repeatedly running the powder derived from serpentine concentrates through the magnetic separator. The product contained a high proportion of the brown material. Still much of the magnetic fraction contained non-magnetic Fe-poor serpentine with embedded brown material. The X-ray diffractogram showed serpentine only and a strongly elevated background. In a further laboratory test, we performed a reaction of the brown material concentrate with 10 % HCl. The brown material instantaneously dissolved in the acid, leaving behind sediment of colorless serpentine. The yellow solution contained iron(III) chloride. We conclude from our observations that the brown stain is X-ray amorphous iron(III) oxide–hydroxide. Its composition can be written as $Fe(OH)_3$ or alternatively as $FeO(OH)\cdot H_2O$. The material is a common naturally occurring low-T precursor of crystalline iron(III) oxides–hydroxides such as ferrihydrite, goethite, and hematite (Schwertmann and Fischer 1973; Fischer and Schwertmann 1975). Aging and crystallizing processes gradually transform amorphous to crystalline phases (Colombo and Violante 1997).

Rocks

The green peridotite has a chemical composition typical of mantle-derived harzburgite and lherzolite (GC = green core in Table 2). The major components are SiO_2 and MgO, which are present in about equal amounts and form together 80 wt% of the rocks. Total iron (as FeO) is about 8 wt%. Minor components are CaO and Al_2O_3 with concentrations below 2 wt%. Typical for the rocks are high Ni and Cr concentrations in the range of 2000–2600 ppm for each element, respectively. The bulk rock X_{Mg} of the four analyzed samples is close to 0.9. The loss on ignition data (LOI) and the computed H_2O concentrations range from 7 to 11 wt%. This corresponds to 45–90 vol.% serpentine in the rocks (ignoring small modal amounts of Fe hydroxide). Computed CIPW normative minerals indicate original rock composition of olivine-rich harzburgite or lherzolite very close to the harzburgite field (Cpx < 5 vol.%). Computed normative orthopyroxene varies from 13 to 17 vol.%.

The composition of the brown weathering rinds on all four samples is very similar to the composition

Table 1 Composition of minerals (wt%)

	Garnet			Spinel		Olivine		Serpentine	
	Grt 1.1 rim	Grt 1.2	Grt 1.3 core	Spl-1	Spl-7	OL 1–1.3	Ol 2–2.1	Srp c2a6 green rock	Srp c2g16 brown rind
SiO_2	42.09	41.97	41.91			40.49	39.96	41.28	41.62
TiO_2	0.24	0.23	0.24					0.00	0.00
Al_2O_3	23.38	23.33	23.26	44.65	42.43			0.02	0.01
Cr_2O_3	0.87	0.80	0.88	24.75	27.44			0.05	0.00
Fe_2O_3	0.92	0.68	0.34						
FeO	7.03	7.62	7.76	12.69	13.00	10.82	13.86	4.11	4.55
MnO	0.32	0.36	0.33	0.12	0.09	0.23	0.42	0.12	0.03
MgO	20.57	20.23	20.13	17.27	16.88	48.04	44.96	38.70	39.36
CaO	5.09	4.96	4.95	0.14	0.22	0.02	0.02	0.07	0.03
NiO						0.32	0.18		
Total	100.53	100.16	99.81	99.65	100.10	99.92	99.40	84.35	85.60
(Oxygen)	12	12	12	4	4	4	4	7	7
Si	2.967	2.974	2.979			1.000	1.007	2.007	1.997
Ti	0.013	0.012	0.013					0.001	0.001
Al	1.942	1.948	1.949	1.452	1.390			0.000	0.000
Cr	0.048	0.045	0.050	0.540	0.603			0.002	0.000
Fe3	0.049	0.036	0.018						
Fe2	0.414	0.451	0.461	0.293	0.302	0.224	0.292	0.167	0.183
Mn	0.019	0.021	0.020	0.003	0.002	0.005	0.009	0.005	0.001
Mg	2.162	2.137	2.133	0.711	0.699	1.770	1.686	2.805	2.816
Ca	0.385	0.376	0.377			0.001	0.001	0.004	0.002
Ni				0.003	0.005	0.006	0.004		
Almandine	13.90	15.12	15.42						
Pyrope	72.54	71.56	71.32						
Grossular	12.21	12.03	12.10						
Spessartine	0.65	0.71	0.66						
Uvarovite	0.30	0.28	0.31						
Andradite	0.31	0.22	0.11						
Mg/(Mg + Fe)	0.84	0.83	0.82	0.71	0.70	0.89	0.85	0.94	0.94

of the original green rocks (Table 2: FZ = frontal zone = brown rind next to green rock, OR = outer rim = brown rind at outcrop surface). However, there is a significant compositional difference between the green serpentinized peridotite and its weathering crust. MgO decreases from the green rock through the brown rind toward the surface. The decrease is about 4 wt% or less relative to the protolith. The trend of MgO is compensated by an increase in SiO_2 through the weathering zone of also 4 wt% or less. Total iron increases in the rind between 0 and 1 wt% relative to the green rocks. The observed trends are uniform and thus significant. There is also a small decrease in CaO in the weathering crust of maximum 0.5 wt%. There is no clear trend in trace element concentrations. Also, LOI shows no steady and consistent trend due to the limits of the analytical method. Aluminum correlates with chromium. The two elements are mainly present in spinel. Al and Cr concentrations in the bulk rock (Table 2) depend on the amount and size of the few spinel grains accidentally present in the analyzed volume of rock. The thickness of the crusts limits the volume of the analyzed rock samples. As a result an Al-conserving reference frame (Carmichael 1968) cannot be used for evaluating gains and losses of the major components Mg and Si.

Computed CIPW norm compositions show these compositional trends are strongly enhanced (Table 2). In two of the weathering rinds, the content of normative Opx is doubled, but in the two other samples, the increase in Opx (hypersthene) is less dramatic but still significant. Olivine decreases significantly from 87 to 65 vol.% in the most extreme sample (Table 2). Clearly, the CIPW Opx/Ol ratio increases from the green rock to the brown rind significantly.

Table 2 Composition of Ronda peridotite and weathering rinds on the peridotite

Sample (KB)	962bI GC	962bII FZ	962bIII OR	962aIII GC	962aII FZ	962aI OR	961aII GC	961aI *R*	961bc GC	961bI *R*	961bII *R*	961bIII *R*	961b IV PYOR
SiO_2	38.75	40.60	40.79	40.75	41.23	41.08	39.05	39.40	40.17	42.28	42.24	41.74	42.28
Al_2O_3	1.05	1.11	0.94	1.15	0.79	0.76	1.60	1.66	1.79	1.88	1.87	0.90	1.89
Fe_2O_{3tot}	7.93	8.30	8.32	7.66	8.25	8.31	7.66	7.61	8.16	8.68	8.41	8.11	9.22
MnO	0.12	0.12	0.12	0.11	0.12	0.11	0.11	0.10	0.12	0.13	0.12	0.12	0.14
MgO	39.53	37.71	37.83	41.65	41.71	41.64	39.72	39.00	39.82	38.58	38.52	41.21	37.64
CaO	1.00	0.98	0.65	0.94	0.65	0.47	1.43	1.57	2.00	1.74	1.74	0.75	1.58
LOI	11.83	11.02	11.42	7.29	6.60	7.34	10.01	10.72	7.00	5.83	6.34	6.36	6.27
Total	100.21	99.84	100.07	99.55	99.35	99.71	99.58	100.06	99.06	99.12	99.24	99.19	99.02
Cr	1956	2208	1912	2553	1793	1717	2367	2327	2496	2288	2415	2064	2362
Co	96	102	106	97	106	107	97	94	99	103	102	109	106
Ni	1964	2091	2202	2040	2304	2320	2022	1974	2032	2392	2389	2352	4083
Zn	34	37	37	34	34	35	35	34	39	38	39	36	41
CIPW norm													
Ol	78.5	66.32	65.34	77.16	76.03	76.04	78.34	75.04	76.74	66.43	65.57	72.91	63.76
Opx	15.75	27.61	30.58	17.45	19.95	21.04	13.4	16	12.54	23.65	24.51	22.51	27.25
Cpx	1.9	1.65	0.52	1.32	0.92	0.22	2.44	2.92	4.38	2.99	3.05	1.09	2.32
Pl	2.87	4.07	3.43	4.07	2.78	2.7	5.82	6.05	6.34	6.53	6.5	3.16	6.66
X_{Mg}	89.88	89.01	89.02	90.65	90.01	89.93	90.24	90.13	89.69	88.56	88.56	90.07	87.92

K, P, Na (below detection limit: Ti max 0.05 wt%)

GC green core, *FZ* frontal zone, *OR* outer rim, *R* rim, *PYOR* porous yellow outer rim, *LOI* loss on ignition

Composition of runoff (surface water)

Methods

Temperature, pH, and electric conductivity were measured in situ. The composition of the water was analyzed by the geochemical laboratories of the University of Freiburg. All anions and the monovalent cations were measured with a DX-120 ion chromatograph (IC) from Dionex. Other cations were analyzed with atomic absorption spectrometry (Vario 6 from Analytik Jena). Silica and boron were determined using photometry (UV/Vis spectrometer Lambda 40 from PerkinElmer). The carbonate species were calculated from acid titration in the laboratory. PHREEQC version 2.14 from Parkhurst and Appelo (1999) was used to compute distribution of species, species activities, mass transfers, and saturation states from the database LLNL.dat.

Composition of water

The surface water samples contain Mg^{2+}, HCO_3^- ($+CO_3^{2-}$), and SiO_{2aq} as major solutes (Table 3). The concentrations of all other solutes are much lower. The composition of the waters varies depending on the geological character of the catchment and the total length of the creek at the sampling spot. *Q*1 and *Q*2 are from pure peridotite catchments, *Q*3 and *R*2 have abundant pyroxenite in the catchment, and *R*1 is from a mixed peridotite–pyroxenite catchment. The two peridotite waters *Q*1 and *Q*2 are pure magnesium carbonate waters with an unusually high concentration of dissolved SiO_2. The high SiO_2 concentration is very uncommon for surface waters. Also the total amount of dissolved solids (TDS) is remarkably high (>500 mg/L) for creeks running through crystalline basement rocks. Water in granitic or gneissic basement catchments has typically low silica concentrations (<20 mg/L SiO_2). Quartz saturation is close to 6 mg/L SiO_2 (at 20 °C). Thus, the Ronda waters (Table 3) are extremely high in dissolved SiO_2 caused by the high solubility and fast dissolution kinetics of olivine (Lasaga et al. 1994). However, molal Mg/Si varies within a narrow range of 3.3–4.0. Dissolved Mg and Si are strongly correlated (Fig. 7). The slope of the best-fit straight line through the origin (Fig. 7) corresponds to a molal Mg/Si ratio of 3.8. Congruent olivine dissolution would produce a Mg/Si ratio of 2, equilibrium with serpentine produces a water with Mg/Si = 1.5 (Fig. 7).

The surface waters are characterized by relatively high pH values, leading to the presence of minor amounts of CO_3^{2-} in addition to the dominant bicarbonate anion. A small amount of sodium is matched by an equivalent amount of chloride. Molal Na/Cl is close to one. Calcium is very low in peridotite waters and only slightly higher in pyroxenite dominated catchments. All other solutes are below the analytical detection limit including dissolved

Table 3 Composition of surface waters from brooks of the Ronda peridotite at Pico de los Reales

	*Q*1	*Q*2	*Q*3	*R*1	*R*2
Locality[a]	Nicola N	Nicola S	SE Reales	A397-1	A397-2
Date	6/14/11	6/14/11	6/14/11	5/24/10	5/26/10
pH	8.5	8.36	8.4	8.42	8.54
Concentration in mg/l					
Ca	0.67	0.93	2.17	4.49	2.73
Mg	79.81	84.23	39.65	67.50	40.40
Na	4.01	5.00	4.09	3.55	1.82
K	0.20	0.30	0.36	0.28	0.20
Fe				0.08	0.06
CO_3	15.19	10.74	6.36	10.74	9.18
HCO_3	365.75	398.58	185.38	311.32	182.69
SO_4	3.70	4.07	2.79	4.27	2.12
Cl	6.71	7.20	5.68	8.17	5.11
NO_3	0.43	0.57	1.35	0.24	2.03
SiO_2	52.76	51.62	26.60	44.40	30.10
TDS	529.23	563.25	274.43	455.05	276.45
Concentration in mmol/l					
Ca	0.017	0.023	0.054	0.112	0.068
Mg	3.284	3.466	1.632	2.778	1.663
Na	0.174	0.217	0.178	0.154	0.079
K	0.005	0.008	0.009	0.007	0.005
Fe				0.001	0.001
CO_3	0.253	0.179	0.106	0.179	0.153
HCO_3	5.994	6.532	3.038	5.102	2.994
SO_4	0.039	0.042	0.029	0.044	0.022
Cl	0.189	0.203	0.160	0.230	0.144
NO_3	0.007	0.009	0.022	0.004	0.033
SiO_2	0.878	0.859	0.443	0.739	0.501
Concentration in meq/l					
Ca	0.033	0.046	0.108	0.224	0.136
Mg	6.569	6.933	3.263	5.556	3.325
Na	0.174	0.217	0.178	0.154	0.079
K	0.005	0.008	0.009	0.007	0.005
Fe				0.003	0.002
CO_3	0.506	0.358	0.212	0.358	0.306
HCO_3	5.994	6.532	3.038	5.102	2.994
SO_4	0.077	0.085	0.058	0.089	0.044
Cl	0.189	0.203	0.160	0.230	0.144
NO_3	0.007	0.009	0.022	0.004	0.033
Charge bal. %	0.063	0.118	0.971	1.370	0.377
SI am. silica	−0.2	−0.2	−0.49	−0.27	−0.44

TDS total dissolved solids, *SI* saturation index amorphous silica

[a] Locality: along road MA8301: *Q*1 NW peak Nicola, *Q*2 W peak Nicola, *Q*3 SE Pico de los Reales; along road A397: *R*1 S Cascajares, *R*2 S Cascajares

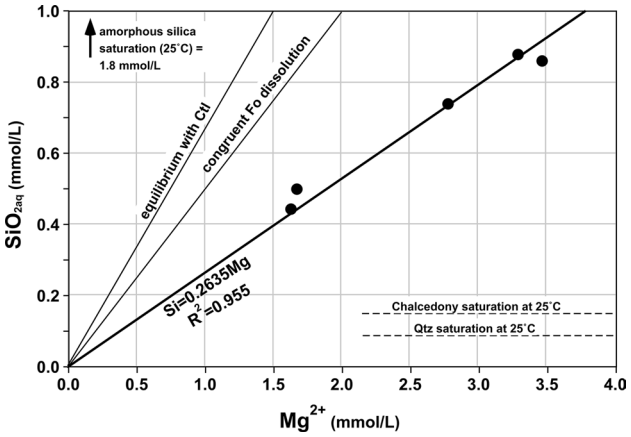

Fig. 7 Dissolved SiO_{2aq} versus Mg^{2+} in surface runoff from the Pico de los Reales area of the Ronda peridotite. Concentration in mmol/L. Linear correlation line through the origin has the Si/Mg slope of 0.2635 corresponding to Mg/Si = 3.8

iron. The composition of high-pH Mg-rich waters has been taken as evidence for ongoing serpentinization in peridotite (Barnes and O'Neil 1971; Barnes et al. 1978).

Discussion

Pre-weathering situation

Before the peridotite reached the erosion surface and started to develop a brown weathering crust, it can be best characterized as a strongly serpentinized spinel harzburgite. The normative orthopyroxene is relatively low (Table 2), and the mineral is present in the four samples as relict. Orthopyroxene has been mostly converted to serpentine during geological periods before reaching the erosion surface. Serpentinization of harzburgite consumed also a part of the primary olivine according to the simplified reaction (1):

$$2Mg_2SiO_4 + 3H_2O = Mg_3Si_2O_5(OH)_4 + Mg^{2+} + 2(OH)^- \quad (1)$$

Note that the process of forsterite to serpentine conversion can be written in many different ways. Here Eq. (1) is Si-conserved with serpentine as reaction product and release of Mg^{2+} to the fluid, which increases in pH with progress of reaction. In a closed system, progress of reaction (1) would slow down when saturation with brucite is approached. However, other processes, as explained below, establish steady-state conditions at constant pH resulting in a steady progress of the serpentinization reaction.

The Fe component of olivine and Opx has been oxidized to magnetite (Eq. 2) indicated by the presence of distributed

small magnetite grains and fine-grained magnetite in the centers of the serpentine veinlets (Figs. 5b, 6a). Magnetite is formed rather than Fe serpentine during serpentinization if aqueous silica in the fluid is low during the process (Frost and Beard 2007; Evans 2008). However, aqueous silica released by the fayalite dissolution produced more serpentine from the forsterite component (Eq. 3).

$$3Fe_2SiO_4 + 2H_2O = 2Fe_3O_4 + 3SiO_{2aq} + 2H_2 \quad (2)$$

$$3Mg_2SiO_4 + SiO_{2aq} + 4H_2O = 2Mg_3Si_2O_5(OH)_4 \quad (3)$$

Modal serpentine in the unweathered rock is in the range of 44–80 % with corresponding amounts of olivine of 18–30 % (Figs. 4, 5). Modal magnetite is below 5 %. The serpentinization process requires H_2O that was taken from an aqueous fluid. The fluid-conducting microstructures are texturally preserved as sutures of the serpentine veinlets. The growth of the veinlets occurred at the olivine–serpentine interface by the combined progress of reactions 1, 2, and 3. The center of the veinlets provided the reactive external fluid. The H_2O has been transported along the serpentine fibers or flakes standing vertical on the central suture to the reaction site at the olivine grain. Fluid transport along the central sutures of the veinlets relates to the aperture of the sutures. The aperture is the perpendicular width of an open fracture or suture. In addition, the flow properties are also influenced by the wall roughness and lateral continuity of the veinlets. The sutures of the veinlets correspond to the positions of the original olivine–olivine grain boundaries. The veinlets developed from H_2O diffusion along these grain boundaries. The specific suture aperture is difficult to quantify; however, it is evident that the suture persists as a water-conducting structure during hydrothermal serpentinization and also during rind formation. Water conduction may occur by Darcy flow, by diffusion or by capillary transport depending on veinlet aperture and availability of external water. Advective flow of water through open vein sutures is a function of the cube of the aperture (cubic law). This mode of transport was probably relevant during the phase of hydrothermal serpentinization.

The temperature at which the hydrothermal serpentinization occurred is difficult to estimate. It was below about 400 °C, because above this temperature, forsterite can be in equilibrium with pure water. It was probably even below 250 °C because below this temperature chrysotile or lizardite is more stable than antigorite (Evans et al. 2013). Serpentinization of the Ronda peridotite was possibly related to the thrusting of the nappe during the collisional episode that formed the Betic cordillera. Active tectonic nappe movement has been dated to 30 Ma that is Miocene time. Thrusting occurred under relatively low total load pressure of less than 300 MPa (Alonso-Chaves et al. 2004).

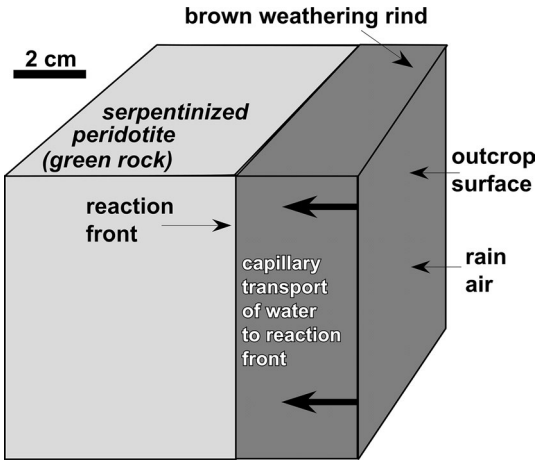

Fig. 8 General schematic setup of rind growth

The weathering crust-forming process

Isostatic rebound and uplift caused denudation of the units covering the Ronda peridotite and exposed the ultramafic rocks to the atmosphere. Since then, periodic rainfall wetted the rock surfaces and the water migrated into the central suture of the serpentine veinlets probably by capillary forces (Fig. 8). The suture remains a water-conducting structure during rind formation. As mentioned, water conduction may occur by Darcy flow, by diffusion or by capillary transport depending on veinlet aperture and availability of external water. Darcy flow is not the transport mechanism during the rind formation. This follows from the geometry and structure of the rinds (Fig. 2). In the context of rind formation, first, water needs to be supplied by capillary transport along open sutures, and then diffusion sets in and distributes H_2O on a fine scale. The reactive rainwater is close to equilibrium with atmospheric O_2 and CO_2 (about 9.4 mg/l O_2 at 20 °C and 0.6 mg/l CO_2, pH = 5.6).

Since the brown stain consists of Fe(III) hydroxide, a source for the iron is needed for producing the stain. Fe is present in primary olivine and Cr-spinel and in hydrothermally produced serpentine and magnetite (Table 1). The rock textures do not support Cr-spinel dissolution during weathering. Because the runoff waters are strongly oversaturated with respect to serpentine (see data and discussion below), serpentine is not a source of Fe for the stain. Magnetite formed during hydrothermal serpentinization could be dissolved and re-precipitated as Fe(III) hydroxide according to the reaction:

$$4Fe_3O_4 + 18H_2O + O_2 = 12Fe(OH)_3 \quad (4)$$

Reaction (4) produces the brown stain by oxidizing and hydrating magnetite grains. Some of the magnetite can be

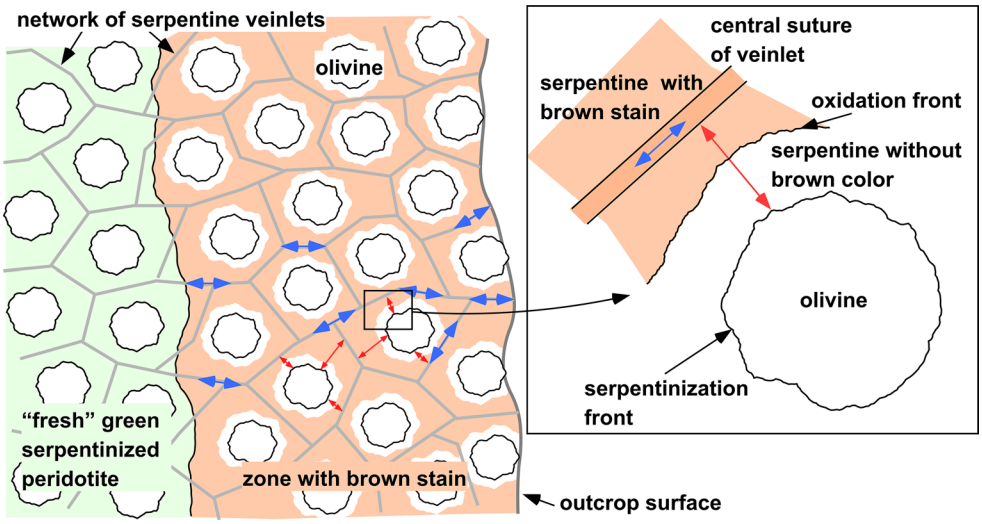

Fig. 9 Schematic textural system of rind growth. Central suture of serpentine veinlets in *gray*, capillary water migration = *blue arrows*, diffusional exchange of components = *red arrows*

found in the central sutures of the veinlets (Fig. 6) where also brown stain is present. However, larger magnetite grains are not texturally related to the brown stain. For example, Fe hydroxide does not mantle magnetite as would be expected if reaction (4) was an important process in stain formation. Furthermore, magnetite grains and aggregates at the weathering surface of serpentinite bodies (incl. Ronda) are not covered with rusty crusts. The solubility of magnetite in rainwater is about 4 µmol/L (PHREEQC; Parkhurst and Appelo 1999), whereas the solubility of olivine is close to 1.9 mol/L. Thus, it can be excluded that the brown color of the crust results from magnetite oxidation. The iron source for the brown stain is the fayalite component of the olivine grains. The Fe(II) of the silicate is released during olivine dissolution and then re-precipitated as Fe(III) hydroxide. The transfer of silicate iron to hydroxide iron can be clearly seen on the BSE images (Fig. 6). In the brown rock, highly reflective Fe hydroxide is abundant. In the green rock, Fe is predominant in silicates and in scattered grains of magnetite. The total iron of the two types of rocks is similar (Table 2).

The olivine dissolution is related to H_2O in the central capillary porosity of the veinlets after a wetting event. The H_2O migrates along the serpentine fibers or sheets to the reaction front at the olivine grain (Fig. 5b, 9). Up to this point, the fluid has been close to equilibrium with serpentine by dissolution of small amounts of the mineral it encounters along the migration path. At the olivine boundary, the aqueous fluid is not in equilibrium with this mineral. Dissolution reactions cannot equilibrate the fluid with olivine at the low surface temperature (Wogelius and Walther 1991; Martinez et al. 2014). A hypothetical solution in equilibrium with forsterite would be massively oversaturated with a number of secondary low-temperature hydrate minerals including serpentine, talc, and sepiolite (PHREEQC; Parkhurst and Appelo 1999). The resulting saturation index $SI_{chrysotile} = 8.5$ at equilibrium with forsterite is likely far above supersaturation required for serpentine growth. Because serpentine is already present in the veinlets, required supersaturation for serpentine (e.g., chrysotile) growth is much lower than critical supersaturation for nucleation of serpentine (Fritz et al. 2009). Thus, it is suggested that olivine dissolution at the reaction front is accompanied by serpentine formation according to a reaction similar to reaction (1). Serpentine may form because the mineral is already present in the rock from the main serpentinization episode as described above. It serves as a nucleation seed for the continuation of serpentinization related to weathering. The major difference to the main serpentinization process is the behavior of the iron component of olivine. The main serpentinization process partly oxidized the Fe(II) to magnetite. The weathering process oxidizes Fe(II) in olivine to an X-ray amorphous Fe(III) hydroxide, the brown stain. Precipitation of brown Fe(III) hydroxide occurs close to and along the central sutures of the chrysotile veinlets (Fig. 5, 6). In the vicinity of the olivine grains, no brown stain is formed, suggesting that the iron is first released as Fe(II) and oxidized on its way to the central suture (Fig. 5b). The detailed and stepwise olivine dissolution and the subsequent oxidation of the Fe(II) in the solution can be described by the following stoichiometric equations:

Olivine dissolution reactions (site 3 Fig. 5b) for Ronda olivine with 88 mol % Fo component and 12 mol % Fa component:

$$\text{Forsterite: } Mg_2SiO_4 + 2H_2O = 2Mg^{2+} + 4OH^- + SiO_{2aq} \quad (5)$$

$$\text{Fayalite: } Fe_2SiO_4 + 2H_2O = 2Fe^{2+} + 4OH^- + SiO_{2aq} \quad (6)$$

Serpentine precipitation (site 3 Fig. 5b)

$$3Mg^{2+} + 6OH^{-} + 2SiO_{2aq} = Mg_3Si_2O_5(OH)_4 + H_2O \quad (7)$$

Amorphous Fe hydroxide precipitation (site 2 Fig. 5b)

$$4Fe^{2+} + 8OH^{-} + O_2 + 2H_2O = 4Fe(OH)_3 \quad (8)$$

Net transfer:

$$\text{Olivine} + H_2O + O_2 = \text{Serpentine} + Fe(OH)_3 + n\,Mg^{2+} + 2n\,OH^{-} + m\,SiO_{2aq} \quad (9)$$

n/m measured in surface water = 3.8 (Table 3).

Iron is fully conserved between the solid reactants and products of reaction (9). The olivine to serpentine + $Fe(OH)_3$ conversion cannot conserve both Mg and Si. The composition of the surface waters shows that components released by olivine dissolution are not quantitatively trapped by serpentine precipitation (n/m = 3.8). Because the Mg/Si ratio in surface water is higher than that of olivine and serpentine, we conclude that the composition of the water does not reflect simple olivine (forsterite) or serpentine dissolution. The water finally arriving at the rock surface by porous capillary flow during the drying cycle is later diluted by rainwater. However, the surface waters (streams, creeks, brooks) still reflect the component ratios of the original pore water in the rock.

The magnesium and silica contents of the runoff waters are strongly correlated (Fig. 7). The slope of the correlation straight line through the origin is close to 3.8 (molar). The strong correlation between Mg and Si seen on Fig. 7 suggests that the release of the two solutes is governed by a single uniform process. Stoichiometric dissolution of Fo or Srp results in corresponding slopes of 2 and 1.5, respectively. Interestingly, the volume-conserved replacement of olivine by serpentine results in a slope of 4.09 if calculated for pure forsterite and serpentine. In such a process, one cm^3 of olivine is replaced by exactly one cm^3 of serpentine. Such an iso-volume replacement is consistent with the observed and documented textures of the crust on peridotite (Fig. 5). The Mg/Si of the volume-conserved olivine–serpentine reaction of an $Fo_{90}Fa_{10}$ olivine centers around 3.7 ± 0.3 depending on the composition of the reaction products such as Fe content of product serpentine. We thus take the data shown on Fig. 7 as a strong evidence for an active volume-conserved serpentinization of olivine, whereby the brown stain of the crust is caused by amorphous Fe hydroxide an oxidation by-product of the serpentinization process. Volume-conserving replacement is common in pseudomorphing reactions metamorphic rocks (Carmichael 1968; Carlson and Johnson 1991). It is evidently also operating in weathering environments.

The saturation index with respect to forsterite of all sampled surface waters varies between −3.47 and −4.00. Thus, there is a continuous chemical driving force for olivine dissolution. The saturation index with respect to chrysotile ranges from 3.7 to 4.5. We conclude that the state of critical supersaturation with respect to serpentine (chrysotile) at surface conditions must be close to these values (~4). All waters are undersaturated with respect to amorphous silica (Table 3) and oversaturated with respect to chalcedony and quartz (Fig. 7). However, the $SI_{Qtz} = 1.2$ in the most silica-rich water is not high enough to precipitate quartz (or chalcedony). Hence, $SI_{Qtz} = 1.2$ appears to be below critical supersaturation with respect to quartz at surface conditions. The absence of any form of silica phase in the pores of the rinds or sinter in the riverbeds suggests that silicification, observed elsewhere (Silantyev et al. 2012), is not an active process in the Ronda peridotite.

The data imply that within the 2- to 3-cm-thick weathering crust, the bulk Ol–Srp reaction releases predominantly $Mg(OH)_2$ resulting in a relatively high pH and Mg/Si ratio in the runoff similar to findings from an ultramafic body in Serbia (Nikic et al. 2013). At the evaporation surface during the drying cycle, dissolved $Mg(OH)_2$ comes in contact with CO_2 from the atmosphere and OH^- is converted to HCO_3^- by the reaction:

$$OH^{-} + CO_2 = HCO_3^{-} \quad (10)$$

The resulting dissolved Mg bicarbonate $Mg(HCO_3)_2$ and the dissolved silica are finally washed to creeks and streams during the next rain (wetting) period.

Since rind thicknesses in similarly serpentinized peridotites from Ronda and from northern Norway (Figs. 2, 3) are about 10–30 mm, it appears that climate effects are of minor importance. Climate refers here basically to mean annual temperature. Annual precipitation is similar at both locations [366 vs. 450 mm/a (yr.no)]. In the winter month, outcrops in northern Norway are frozen and snow covered, and in the Ronda area, rain minimum is in the hot summer months. Thus, rind growth is probably at its maximum during summer in Norway and during the winter month in the Ronda area. Because rind thicknesses vary from 1–2 mm in dunite to 10–20 mm on serpentinized dunites or harzburgites from northern Norway (Figs. 1a, 2), we conclude that the texture and structure of the peridotite is more important than climate in the development of the rinds in temperate to boreal climates.

The data from the runoff water and observation of the rind structure imply that there is an efficient transport mechanism for water and dissolved components from the reaction site at the brown–green interface to the surface of the rocks and finally to the surface water.

The data also suggest that the most significant chemical reaction takes place at the olivine–serpentine interface. This means that transport and reaction needs to be considered in separate small scale compartments (Fig. 9). Transport of components to and from the olivine interface

to the central suture of the veinlets is by diffusion. Transport along the central suture and the associated pore space is accomplished by capillary fluid flow during the drying phase of the wetting and drying cycle. During the liquid-saturated period, diffusion may also contribute to component transport in the pore space.

The details of solute transport on a microscopic scale and the component release to the surface water are related to transport processes associated with the wetting and drying mechanism (including capillary rise, infiltration, and drainage). The description of these transport mechanisms involving moving menisci depends on the quantitative account of the pore space on a microscopic scale (van Brakel 1975). The thickness of the developed rinds relates to the local fine structure of the porosity. It is strongly influenced by microfractures providing enhanced porosity (Fig. 2).

After a wetting period, the interconnected porosity of the partly serpentinized peridotite is saturated with water. During a subsequent drying stage, first evaporation takes place at the surface of the rock, later on somewhere inside the porous rock. Several transport processes take place. Heat flows from the atmosphere and the rock surface to the place of evaporation. Diffusion of water vapor occurs in the opposite direction. As long as the liquid phase in the porous rock is continuous, there will be transport of liquid and its dissolved components to the place of evaporation, induced by capillary forces. During the succeeding liquid saturation stage, the dissolved solids can be released to the rainwater wetting the rock surface.

An interesting question remains: What is the rate of rind growth for the Ronda peridotite? It is possible to attempt a theoretical growth model that considers reaction kinetics and transport processes, e.g., with the code THOUGHREACT (Xu et al. 2006). The code can model capillary transport. However, most of the required input parameters are only vaguely known so that the model can produce any plausible or implausible result. More realistic are direct observations at road cuts and peridotite quarries. The visited road cuts in the Ronda Peridotite are typically younger than 50 years. All road cuts show yellow crusts, and no green road cuts exist. We conclude from this observation that the first thin yellow rind develops very rapidly. Then crust growth slows down and crust thickness may reach 20–30 mm after 30–40 years. This would convert to crust growth rates on the order of 0.5–1.0 mm/a during the first decades of exposition to the atmosphere. These rates, however, are restricted to serpentinized peridotites. Crust growth rates on pure dunites are much lower because fluid migration along olivine–olivine grain boundaries is much less efficient than fluid migration along the central sutures of serpentine veinlets.

Conclusions

The intensive and characteristic brown color stain of weathering rinds of peridotite surface outcrops is caused in the studied occurrences by X-ray amorphous Fe(III) hydroxide precipitates resulting from olivine dissolution in surface water and subsequent oxidation of Fe(II) to Fe(III) in the solution. The total amount of brown Fe(III) hydroxide is small; however, the material appears to be extremely color dominant. The kinetics of the Fe(II) to Fe(III) oxidation (Geroni and Sapsford 2011) occurs in an aqueous liquid phase and thus is correspondingly fast. However, the growth of the rind is controlled by the structure of the serpentinized peridotite. The critical step appears to be wetting of the reactive system by precipitation water. The H_2O-transporting process appears to be capillary transport (Fig. 8) in the Ronda samples.

Porosity formation by chemical dissolution of silicates is a key mechanism providing transport paths for surface water (rain water) and dissolved components (Jin et al. 2011; Weisenberger and Bucher 2011) that finally can be found in the discharge after rainfall events. Wetting and drying cycles provide first liquid saturation of the pore space and then an efficient transport mechanism of liquid and dissolved components to the surface of the rock. The derived chemical net reaction suggests ongoing serpentinization during weathering. A similar bulk process has recently been suggested for peridotite at the Knipovich Ridge in the Arctic Ocean (Rajan et al. 2012). The structural and textural details of the brown weathering rinds on the Ronda peridotite together with the composition of runoff water can be best explained by a transport-controlled combined volume-conserving serpentinization–oxidation process.

Present-day serpentinization is thus a general process being active wherever peridotite is exposed at the surface and olivine is in contact with H_2O at low temperature. The mechanism of reaction front propagation, where green rock is converted to brown rock has remarkable similarities to the growth of reaction veins in metamorphic rocks (Bucher-Nurminen 1981; Stober and Bucher 2015). The growth of both structures, brown rind and vein rocks, is caused by the reaction of a fluid with a mineral assemblage with which this fluid is not in equilibrium. Initially, the growth of the alteration zone is controlled by the kinetics of the alteration reaction; later when the reacted zone gets thicker growth (propagation of the reaction front), it becomes transport-controlled (Bucher 1998).

Acknowledgments Antonio Carcia-Casco from the University of Granada provided precise information on the localities of garnet peridotite in the Ronda massif. His responsive help is gratefully acknowledged. Careful reviews by Bernard Evans, Ralf Milke, and an anonymous reviewer are appreciated. We also thank Chris Ballhaus for his mindful editorial handling of the manuscript.

References

Alonso-Chaves FM, Soto JI, Orozco M, Kilias AA, Tranos MD (2004) Tectonic evolution of the betic cordillera: an overwiew. Bull Geol Soc Greece 36:1598–1607

Barnes I, O'Neil JR (1971) The relationship between fluids in some fresh Alpine-type ultramafics and possible modern serpentinization, Western United States. Bull Geol Soc Am 80:1947–1960

Barnes I, O'Neil JR, Trescases JJ (1978) Present day serpentinization in New Caledonia, Oman and Yugoslavia. Geochim Cosmochim Acta 42(1):144–145

Boev B, Jovanovski G, Makreski P (2009) Minerals from Macedonia. XX. Geological setting, lithologies, and identification of the minerals from Ržanovo Fe-Ni deposit. Turk J Earth Sci 18:631–652

Bucher K (1998) Growth mechanisms of metasomatic reaction veins in dolomite marbles from the Bergell Alps. Mineral Petrol 63:151–171

Bucher K (2012) Progress of weathering reactions in ultramafic rocks. Goldschmidt 2012 conference abstracts, minerological magzine, p 1523

Bucher K, Grapes R (2011) Petrogenesis of metamorphic rocks. Springer, Berlin, p 428

Bucher-Nurminen K (1981) The formation of metasomatic reaction veins in dolomitic marble roof pendants in the Bergell intrusion (Province Sondrio, Northern Italy). Am J Sci 281:1197–1222

Bucher-Nurminen K (1991) Mantle fragments in the Scandinavian Caledonides. Tectonophysics 190:173–192

Carlson WD, Johnson CD (1991) Coronal reaction textures in garnet amphibolites of the Llano Uplift. Am Miner 76:756–772

Carmichael D (1968) On the mechanism of prograde metamorphic reactions in quartz-bearing pelitic rocks. Contrib Miner Petrol 20:244–267

Colombo C, Violante A (1997) Effect of ageing on the nature and interlayering of mixed hydroxy A1–Fe-montmorillonite complexes. Clay Miner 32:55–64

Dikey JS, Lundeen MT, Obata M (1979) Geologic map of the ultramafic complex, southern Spain. In: Geological society of America map and chart series MC-29. Geological Society of America, Boulder, pp 1–4

Dixon JC, Thorn CE, Darmody RG, Campbell SW (2002) Weathering rinds and rock coatings from an Arctic alpine environment, northern Scandinavia. Geol Soc Am Bull 114:226–238

Durocher JL, Schindler M (2011) Iron-hydroxide, iron-sulfate and hydrous/silica coatings in acid-mine tailings facilities A comparative study of their trace-element composition. Appl Geochem 26:1337–1354

Edwards AB (1938) The formation of iddingsite. Am Miner 23:277–281

Evans BW (2008) Control of the products of serpentinization by the $Fe^{2+}Mg_{-1}$ exchange potential of olivine and orthopyroxene. J Petrol 49:1873–1887

Evans KA, Powell R, Frost BR (2013) Using equilibrium thermodynamics in the study of metasomatic alteration, illustrated by an application to serpentinites. Lithos 168–169:67–84

Evzerov V, Pripachkin P, Dudkin K (2007) Linear weathering crust of the Fedorova-Pana layered complex in the northeastern Baltic Shield. Dokl Earth Sci 413(1):170–172

Fischer WR, Schwertmann U (1975) The formation of hematite from amorphous iron(III) hydroxide. Clays Clay Miner 23:33–37

Fritz B, Clément A, Amal Y, Noguera C (2009) Simulation of the nucleation and growth of simple clay minerals in weathering processes: the NANOKIN Code. Geochimica et Cosmochim Acta 73:1340–1358

Frost BR, Beard JS (2007) On silica activity and serpentinization. J Petrol 48:1351–1368

Geroni JN, Sapsford DJ (2011) Kinetics of iron (II) oxidation determined in the field. Appl Geochem 26:1452–1457

Jin L, Rother G, Cole DR, Mildner DFR, Duffy CJ, Brantley SL (2011) Characterization of deep weathering and nanoporosity develepment in shale—a neutron study. Am Miner 96(4):498–512

Lasaga AC (1984) Chemical kinetics of water–rock interactions. J Geophys Res 89(B6):4009–4025

Lasaga AC, Soler JM, Ganor J, Burch TE, Nagy KL (1994) Chemical weathering rate laws and global geochemical cycles. Geochim Cosmochim Acta 58:2361–2386

Lauder WR (1965) The geology of Dun Mountain, Nelson, new Zealand part 2—the petrology, structure, and origin of the ultrabasic rocks. NZ J Geol Geophys 8(1):475–504

Lelong F, Tardy Y, Grandin G, Trescases JJ (1976) Pedogenesis, chemical weathering and processes of formation of some supergene ore deposits. In: Wolf KL (ed) Handbook of strata-bound and stratiform ore deposits, vol 3. Elsevier, Amsterdam, pp 93–173

Lindahl I, Nilsson LP (2008) Geology of the soapstone deposits of the Linnajavri area, Hamarøy, Nordland, north Norwegian Caledonides—Norway's largest reserves of soapstone. In: Slagstad T (ed) Geology for society, Geological survey of Norway Special Publication, vol 11, pp 19–35

Martinez R, Weber S, Bucher K (2014) Quantifying the kinetics of olivine dissolution in partially closed and closed batch reactor systems. Chem Geol 367:1–12

Mazzoli S, Martin Algarra A (2011) Deforrmation partitioning during transpressional emplacement of a 'mantle extrusion wedge': the Ronda peridotites, western Betic Cordillera, Spain. J Geol Soc 168:373–382

Mumpton FA, Thompson CS (1966) The stability of brucite in the weathering zone of the New Idria serpentinite. In: Fourteenth national conference on clays and clay minerals, Berkeley, CA, USA, pp 249–257

Nikić Z, Srećković-Batoćanin D, Burazer M, Ristić R (2013) A conceptual model of mildly alkaline water discharging from the Zlatibor ultramafic massif, western Serbia. Hydrogeol J 21:1147–1163

Nilsson LP, Roberts D, Ramsay DM (2005) The Raudfjellet ophiolite fragment, Central Norwegian Caledonides: principal lithological and structural features. Geol Soc Bull 445:101–117

Obata M (1980) The Ronda Peridotite: Garnet–, Spinel–, and Plagioclase-Lherzolite Facies and the P-T Trajectories of a high-temperature mantle intrusion. J Petrol 21:533–572

Parkhurst DL, Appelo CAJ (1999) User's guide to PHREEQC (version 2)—a computer program for speciation, batchreaction, one dimensional transport, and inverse geochemical calculations. In: Water-resources investigations report 99-4259, U.S. Geological Survey, Denver, pp 312

Pouchou G, Pichior F (1991) Quantitative analysis of homogeneous or stratified microvolumes applying the model of "PAP". In: Heinrich KFJ, Newbiry DE (eds) Electron probe quantitation. Plenum Press, New York, pp 31–75

Rajan A, Mienert J, Bünz S (2012) Potential serpentinization, degassing, and gas hydrate formation at a young (<20 Ma) sedimented ocean crust of the Arctic Ocean ridge system. J Geophys Res 117(B3):1–14

Sagapoa CV, Imai A, Watanabe K (2011) Laterization process of ultramafic rocks in Siruka, Solomon Islands. J Nov Carbon Resour Sci 3:32–39

Schubert W (1977) Reaktionen im alpinotypen Peridotitmassiv von Ronda (Spanien) und seinen partiellen Schmelzprodukten. Contrib Miner Petrol 62:205–220

Schubert W (1982) Comments on 'The Ronda Peridotite: Garnet-, Spinel-, and Plagioclase-Lherzolite Facies and the *P*—*T* trajectories of a high-temperature mantle intrusion' by M. Obata (J Petrol 21:533–572, 1980). J Petrol 23:293–295

Schwertmann U, Fischer WR (1973) Natural 'amorphous' ferric hydroxide. Geoderma 10:237–247

Silantyev SA, Novoselov AA, Krasnova EA, Portnyagin MV, Hauff F, Werner R (2012) Silicification of peridotites at the stalemate fracture zone (Northwestern Pacific): reconstruction of the conditions of low-temperature weathering and tectonic interpretation. Petrology 20:21–39

Smith KL, Milnes AR, Eggleton RA (1987) Weathering of basalt: formation of iddingsite. Clays Clay Miner 35:418–428

Stober I, Bucher K (2015) Hydraulic conductivity of fractured upper crust: insights from hydraulic tests in boreholes and fluid-rock interaction in crystalline basement rocks. Geofluids 15:161–178

van Brakel J (1975) Capillary liquid transport in porous media. Doctoral dissertation (unpublished), Technical University of Delft, Netherlands, pp 154

Van der Wal D, Vissers LM (1996) Structural petrology of the Ronda Peridotite, SW Spain: deformation history. J Petrol 37:23–43

Weisenberger T, Bucher K (2011) Mass transfer and porosity evolution during low temperature water–rock interaction in gneisses of the Simano nappe: Arvigo, Val Calanca, Swiss Alps. Contrib Miner Petrol 162:61–81

Wogelius RA, Walther JV (1991) Olivine dissolution at 25°C: effects of pH, CO_2 and organic acids. Geochim Cosmochim Acta 55(4):943–954

Xu T, Sonnenthal E, Spycher N, Pruess K (2006) TOUGHREACT—a simulation program for non-isothermal multiphase reactive geochemical transport in variably saturated geologic media: applications to geothermal injectivity and CO_2 geological sequestration. Comput Geosci 132:145–165

Yoshida H, Metcalfe R, Nishimoto S, Yamamoto H (2011) Weathering rind formation in buried terrace cobbles during periods of up to 300ka. Appl Geochem 26:1706–1721